

A Robust Eco-compatible Microporous Iron Coordination Polymer for CO₂ capture.

Marvin Benzaqui,^{a,b} Mohammad Wahiduzzaman,^c Heng Zhao,^b Md Rafiul Hasan,^{d,e} Timothy Steenhaut,^f Ali Saad,^a Jérôme Marrot,^a Périne Normand,^g Jean-Marc Grenèche,^h Nicolas Heymans,^g Guy De Weireld,^g Antoine Tissot,^b William Shepard,ⁱ Yaroslav Filinchuk,^f Sophie Hermans,^f Florent Carn,^j Magdalena Manlankowska,^{d,e} Carlos Téllez,^{d,e} Joaquín Coronas,^{d,e} Guillaume Maurin,^c Nathalie Steunou,^{a,b*} Christian Serre.^{a,b*}

a. Institut Lavoisier de Versailles, UMR CNRS 8180, Université de Versailles St Quentin en Yvelines, Université Paris Saclay 78000 Versailles, France.

b. Institut des Matériaux Poreux de Paris, ENS, ESPCI Paris, CNRS, PSL university 75005 Paris, France.

c. ICGM, Univ. Montpellier, CNRS, ENSCM, Montpellier, France.

d. Instituto de Nanociencia y Materiales de Aragón (INMA), CSIC-Universidad de Zaragoza, Zaragoza 50018, Spain.

e. Chemical and Environmental Engineering Department, Universidad de Zaragoza, Zaragoza 50018, Spain.

f. Institute of Condensed Matter and Nanosciences, Université catholique de Louvain, 1348 Louvain-la-Neuve, Belgium.

g. Service de Thermodynamique et de Physique Mathématique, Faculté Polytechnique de Mons, Université de Mons, 7000 Mons, Belgium.

h. Institut des Molécules et des Matériaux du Mans, UMR CNRS 6283, Université du Maine, 72085 Le Mans, France.

i. Synchrotron SOLEIL-UR1, Orme des Merisiers, Saint-Aubin, BP 48, 91192 Gif-sur-Yvette, France.

j. Laboratoire Matière et Systèmes Complexes (MSC), UMR CNRS 7057, Université Paris Diderot, Bât. Condorcet, 10 rue A. Domon et L. Duquet, 75013 Paris, France.

Supplementary Information

I- Synthesis and characterization of MIL-178(Fe)

Reflux Synthesis of MIL-178(Fe)-re. MIL-178(Fe)-re microcrystals were synthesized by reflux in water. 1,2,4-BTC (1.05 g, 5 mmol) and anhydrous FeCl₃ (0.81 g, 5 mmol) were poured into a 100 mL round-bottom flask with 50 mL of deionized H₂O. The red mixture was then heated to reflux under stirring. After 16h, the red solution has turned yellow and the mixture was washed with water and ethanol and then filtered to recover a bright yellow powder.

Methods and characterizations. X-ray powder diffraction patterns (XRPD) were collected using Bruker D8 diffractometer mounted with a rotating capillary (θ - 2θ) with Cu radiation ($\lambda_{K\alpha 1} = 1.54059 \text{ \AA}$). N₂ porosimetry experiments were recorded by using a BELSORP-Max porosimeter at 77 K. Thermogravimetric analyses (TGA) were performed on a Perkin Elmer SDA 6000 apparatus. Solids were heated up to 600°C with a heating rate of 2 °C.min⁻¹ in an oxygen atmosphere. SEM images of MIL-178(Fe) crystals have been recorded on a JEOL JSM-7001F microscope equipped with an X-ray energy-dispersive spectrometry (XEDS) detector with a X-Max SDD (Silicon Drift Detector) by Oxford using gold-coated samples. Samples were analysed by FT-IR spectroscopy by using a Nicolet 6700 FTIR spectrometer equipped with a DTGS detector. TEM samples were prepared by drop-casting the MIL-78(Fe) solution on a 200 mesh carbon-coated copper TEM grid. TEM images were acquired on a JEOL 2010 TEM microscope operating at 200 kV.

II-Structure determination by single-crystal X-ray diffraction

Synchrotron-based single-crystal structure resolution. Single crystal X-ray diffraction data were collected on the beamline PROXIMA 2A at Synchrotron SOLEIL, which is tunable in the range from 6 – 17 keV and focuses a maximum flux in excess of 10¹² photons/s into a Gaussian-shaped spot size of 10*5 μm (H*V, FWHM). To reduce the background scatter, the X-ray beam edges are trimmed with a 50 μm pinhole and guard collimator just upstream of the sample. The flux is monitored continuously on the beamline using X-ray beam position monitors, which were calibrated to the flux at the sample position using a calibrated silicon photodiode (AXUV 100, 10 mm × 10 mm active area, 52 μm thick silicon, Opti Diode Corporation). The instrumentation of the experimental station includes a high-performance goniometer (Micro-Diffractometer MD2, MAATEL-ARINAX, France), comprising a high precision air bearing rotation axis and sub-micron resolution centring tables, and an On-Axis-Viewing microscope, which permits visualizing the sample in the same orientation as the X-ray beam. By inserting a scintillator in place of the sample, users can precisely determine the position of the X-rays to within less than a micron, which permits micro-crystals to be well-centred in the X-ray beam and allows users to check for any eventual drifts in X-ray beam position relative to the sample over time. The area detector used for recording diffraction images was an ADSC Q315 area detector (Area Detector Systems Corp., USA). This detector is a

fibre-optic coupled CCD system, which can only readout images (300 ms) while unexposed to X-rays and thus can only operate in shuttered mode.

Data collection and data processing. All of the X-ray diffraction data were collected at $\lambda = 0.73319 \text{ \AA}$ (16.91 keV) in order to collect the Bragg reflections up to and beyond 1.0 \AA resolution. All data were collected from crystals mounted on nylon loops (Mitagen, USA; Molecular Dimensions, UK and Hampton, USA) and kept at 100 K with a CryoStream 700 (Oxford Cryosystems, UK). As the crystals can be difficult to centre visually due to either their small size (few microns) or to optical effects induced by any surrounding mother liquor or oil, all of the samples were aligned with X-rays, whereby a series of diffraction images were collected while the sample was translated perpendicularly to both the X-ray beam and the rotation axis at four orthogonal values of the omega axis. Once centred, X-ray diffraction data were collected in rotation steps of 0.1° over a total range of 360° in omega-axis. The X-ray diffraction images were indexed, integrated and scaled using the XDS package (Kabsch, 2010ab) via the XDSME script (<https://github.com/legrandp/xdsme>). Data were then reformatted (xdsconv.py) and the crystal structures solved using SHELX package (Sheldrick, 2007).

Crystallographic data. Estimated crystal dimensions $10 \mu\text{m} \times 5 \mu\text{m} \times 5 \mu\text{m}$. Data collection parameters: X-ray wavelength 0.73319 \AA ; 0.1 s exposure per image; 3600 images; 0.1° oscillation range; total angular sweep 360° . Values in parentheses are for the outer resolution shell. The crystallographic data of MIL-178(Fe) have been deposited at the Cambridge Crystallographic Data Centre as supplementary publication no. CCDC 2112974.

III-Characterization of MIL-178(Fe)-hyd by ^{57}Fe Mössbauer spectroscopy.

The powdered sample containing about 5 mg Fe/cm^2 was placed either in a bath cryostat or in a homemade cryofurnace to check the influence of the environment as a function of temperature. Mössbauer measurements were performed at 300 and 77 K using a $^{57}\text{Co/Rh}$ γ -ray source with an activity of about 1.5 GBq and mounted on a conventional constant acceleration vibrating electromagnetic transducer. The spectra were described by means of quadrupolar doublets with lorentzian lines using the Mosfit program.¹

IV-Characterization of MIL-178(Fe) samples

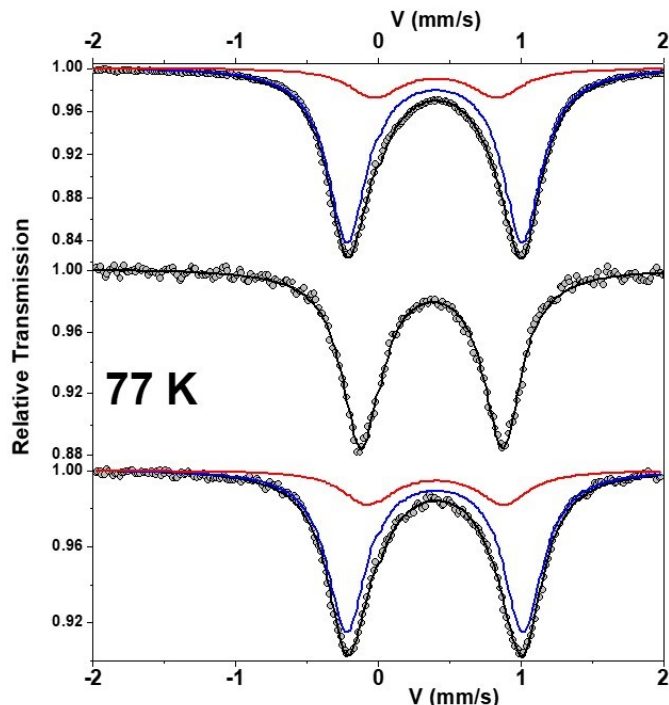


Fig. S1 : ^{57}Fe Mössbauer spectra obtained at 77 K of the as-prepared MIL-178(Fe)-hyd, (top), under vacuum after controlled heating (middle) and after exposure to room atmosphere (bottom).

The Mössbauer spectra at 300 K and 77 K obtained on the as-prepared MIL-178(Fe)-*hyd* (only the 77 K spectrum is shown in the upper Fig. S1) consists of a quadrupolar structure that cannot be perfectly described by means of a single component, as expected from the crystal structure. A second additional Γ_2 component (estimated at about 17% of the total absorption area at 300 and 77 K) must be considered: the total hyperfine structure is consistent with the presence of 2 high spin state Fe^{3+} species. In a second step, measurements were performed under vacuum using the cryofurnace. We first observe a slight decrease in the quadrupolar splitting and in the relative proportion of the second component Γ_2 at 300 K and 77 K, compared to previous measurements. Complementary spectra were obtained after keeping the powder *in situ* at 60°C and 100°C for one 1h in the cryofurnace: the Mössbauer spectrum illustrated in the middle of Fig. S1 clearly shows a single quadrupolar component attributed to the presence of Fe^{3+} species: it is important to note that the quadrupolar splitting is significantly decreased (as shown in Fig. S1). The last step was to put the MIL-78(Fe)-*hyd* sample under ambient atmosphere for about 24h. The hyperfine structures at 300 and 77 K become similar to those observed on the as-prepared sample (see bottom Fig. S1). This series of spectra performed in different environmental conditions clearly demonstrates the presence of water molecules in the as-prepared MIL-178(Fe)-*hyd* sample; their departure occurs when the pressure is decreased and/or the sample heated under vacuum with a small but reversible distortion of the local structure. Such a phenomenon has already been observed on ULM-14 and MIL-82 materials^{2,3} and revealed by local and *in situ* ^{57}Fe Mössbauer spectrometry studies.

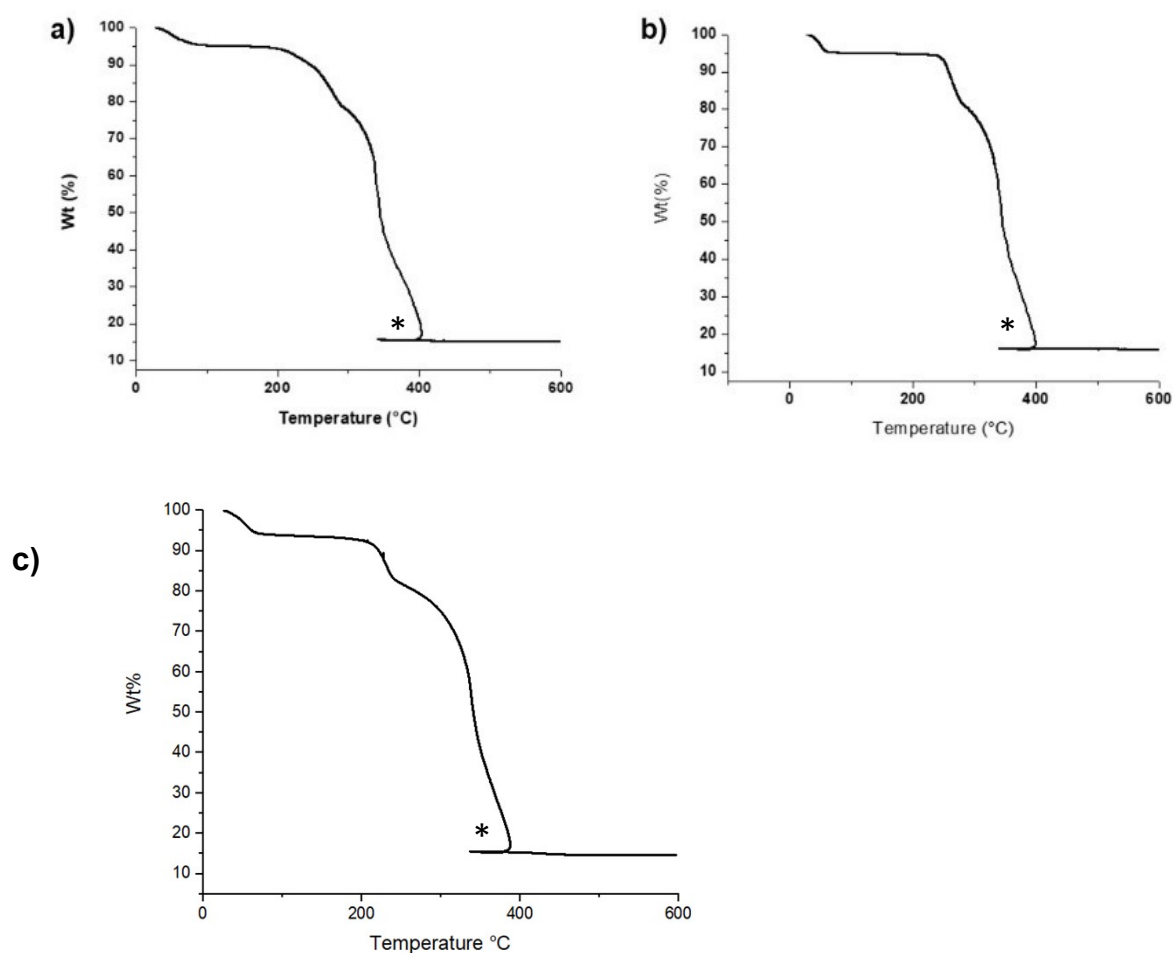


Fig. S2. TGA of (a) MIL-178(Fe)-*hyd*, (b) MIL-178(Fe)-*re*, (c) MIL-178(Fe)-*RT*. The lag in temperature shown by an asterisk * is due to the strong exothermic reaction related to the combustion of the organic linker of the MOF.

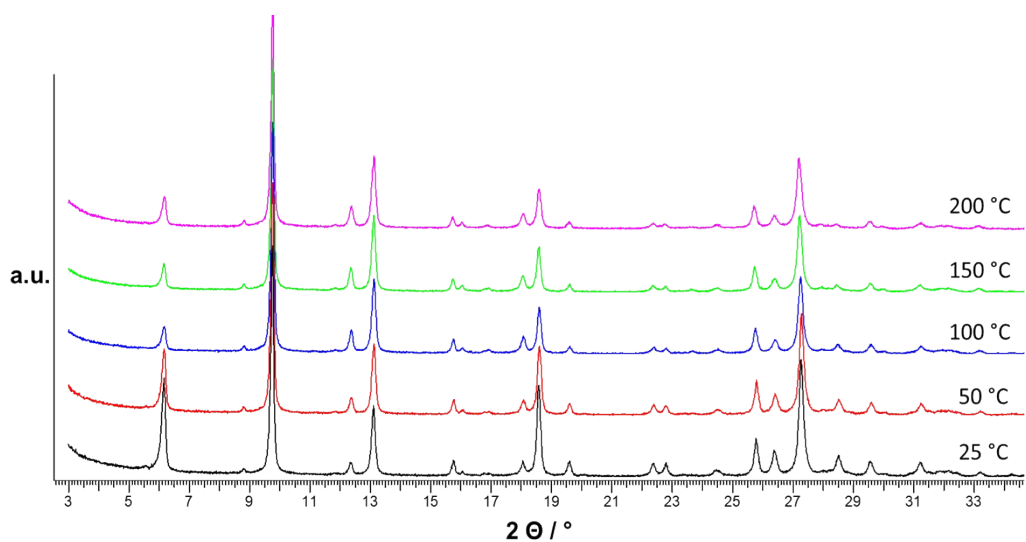


Fig. S3. Temperature dependent PXRD pattern of MIL-178(Fe)-*hyd*.

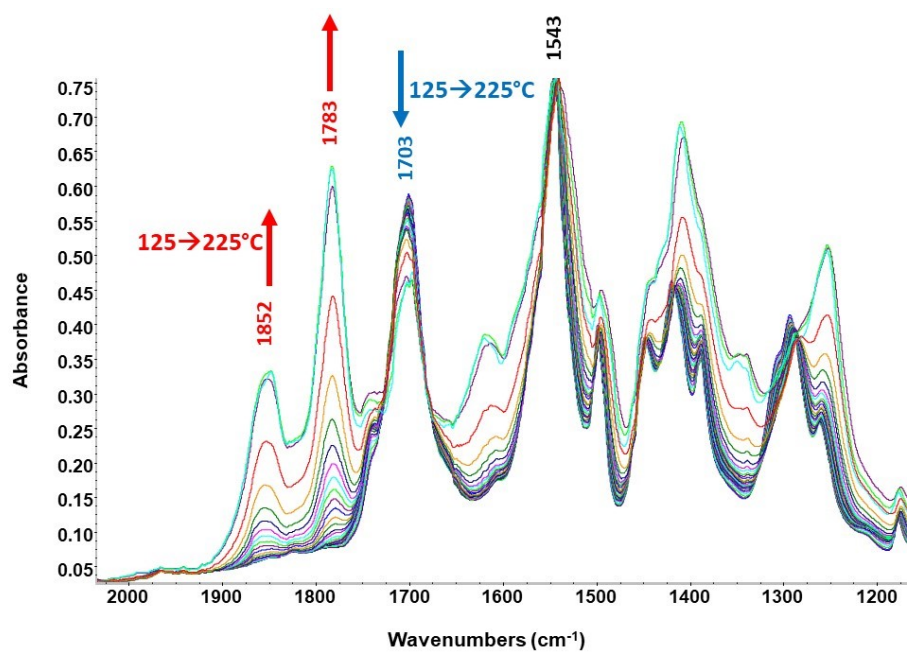


Fig. S4. Temperature-dependent FT-IR spectra of MIL-178(Fe)-*hyd*.

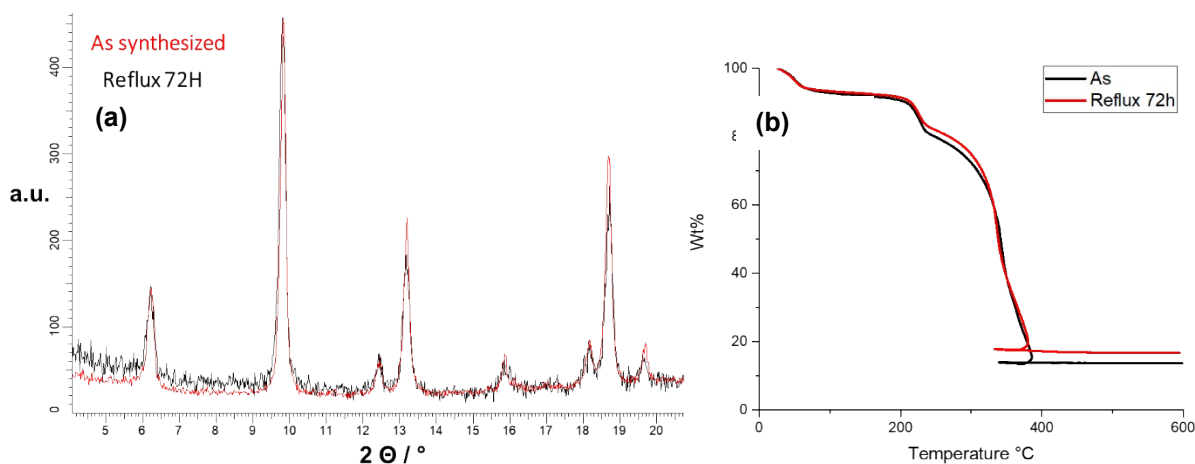


Fig. S5. (a) PXRD pattern and (b) TGA of MIL-178(Fe)-*hyd* before and after hydrothermal stability test (reflux in water for 72h).

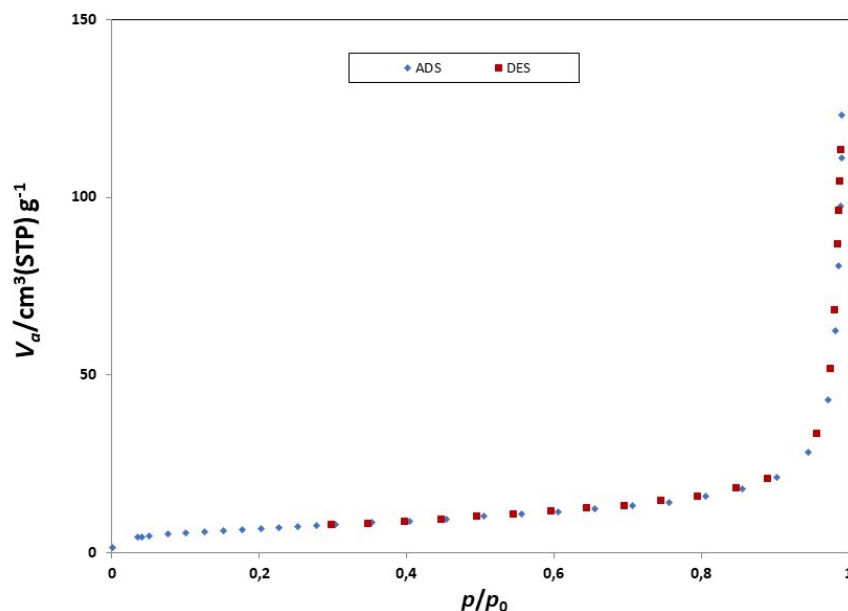


Fig. S6. N_2 adsorption isotherm of MIL-178(Fe)-*hyd* at 77 K.

IV-Molecular Simulations

DFT Calculations. The periodic DFT calculations to optimize the MIL-178(Fe) structure models were performed using the Quickstep module⁴ of the CP2K program^{5,6} employing the Gaussian Plane Wave (GPW) formalism. The general gradient approximation (GGA) to the exchange-correlation functional according to Perdew-Burke-Ernzerhof (PBE)⁷ was used in combination with Grimme's DFT-D3 semi empirical dispersion corrections.^{8,9} Molecularly optimized Triple- ζ plus valence polarized Gaussian-type basis sets (TZVP-MOLOPT) were considered for all atoms, except for the Fe metal centers, where shorter-range double- ζ plus valence polarization functions (DZVP-MOLOPT) were employed.¹⁰ The interactions between core electrons and valence shells of the atoms were described by the pseudopotentials derived by Goedecker, Teter, and Hutter (GTH).^{11,12,13} The auxiliary plane wave basis sets were truncated at 400 Ry. These DFT calculations allowed to extract the atomic partial charges from the CP2K derived electron densities with the DDEC (Density-Derived Electrostatic and Chemical charges) method using the DDEC6 program.^{14,15,16}

Monte Carlo simulations. Force field grand canonical Monte Carlo (GCMC) simulations were performed at 298 and 303 K to assess the single component CO_2 and N_2 and binary mixture CO_2/N_2 (15/85 molar compositions) in MIL-178(Fe). These calculations were performed by Adsorption and Diffusion Simulation Suite (CADSS) code.¹⁷ We considered a simulation box made of $7 \times 2 \times 5$ unit cells maintaining atoms at their initial positions. The interactions between the guest CO_2/N_2

molecules with the MOF structure were described by a combination of site-to-site Lennard-Jones (LJ) contribution and Coulombic term. The universal force field (UFF) parameters were adopted to describe the LJ parameters for the atoms of the framework (see **Table S1**). The CO₂ and N₂ molecules were described by the TraPPE potential models.¹⁸ In this simulation, hydrogen atoms of the –CO₂H and μ-OH species were set to interact with the adsorbate CO₂/N₂ molecules via the Coulombic potential only. Short-range dispersion forces were truncated at a cutoff radius of 12 Å while the interactions between unlike force field centers were treated by means of the Lorentz-Berthelot combination rule. The long-range electrostatic interactions were handled using the Ewald summation technique. The fugacities for each adsorbed species at a given thermodynamic condition were computed with the Peng-Robinson equation of state (EoS).¹⁹ For each state point, 1×10⁷ and 2×10⁷ Monte Carlo steps have been used for equilibration and production runs, respectively. The adsorption enthalpy at low coverage (Δh) for each gas was calculated through configurational-bias Monte Carlo simulations performed in the NVT ensemble using the revised Widom's test particle insertion method. Additionally, in order to gain insight into the configurational distribution of the adsorbed species in MIL-178(Fe), some additional data were calculated at different pressure including the radial distribution functions (RDF) between the guests and the host.

Pore volume and Pore size distribution (PSD). The pore volume and pore size distribution of the geometric topology of the MIL-178 were calculated using zeo++ software.²⁰ For the atoms of the frameworks, default definition of the atomic radii as recorded in the software was used. The free pore volume (V_{pore}) of the frameworks was calculated using the same geometric method but with a probe molecule of 0 Å.

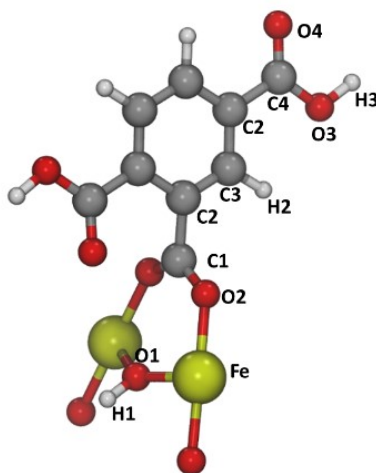


Fig. S7. A representative fragment of the MIL-178(Fe) system highlighting the different atom types in which forced field parameters and DFT derived atomic partial charges were assigned.

Table S1. LJ potential parameters and atomic partial charges of the MIL-178(Fe) framework atoms. Due to some degrees of fluctuations, DFT derived atomic charges for a similar chemical environment was averaged.

| Atom types | σ [Å] | ϵ/k_B [K] | q (e ⁻) |
|------------|--------------|--------------------|-----------------------|
| C1 | 3.431 | 52.839 | 0.609 |
| C2 | 3.431 | 52.839 | -0.037 |
| C3 | 3.431 | 52.839 | -0.088 |
| C4 | 3.431 | 52.839 | 0.582 |
| Fe | 2.594 | 6.542 | 1.080 |
| H1 | 2.571 | 0 | 0.425 |
| H2 | 2.571 | 22.142 | 0.120 |
| H3 | 2.571 | 0 | 0.364 |
| O1 | 3.118 | 30.194 | -0.665 |
| O2 | 3.118 | 30.194 | -0.504 |
| O3 | 3.118 | 30.194 | -0.459 |
| O4 | 3.118 | 30.194 | -0.490 |

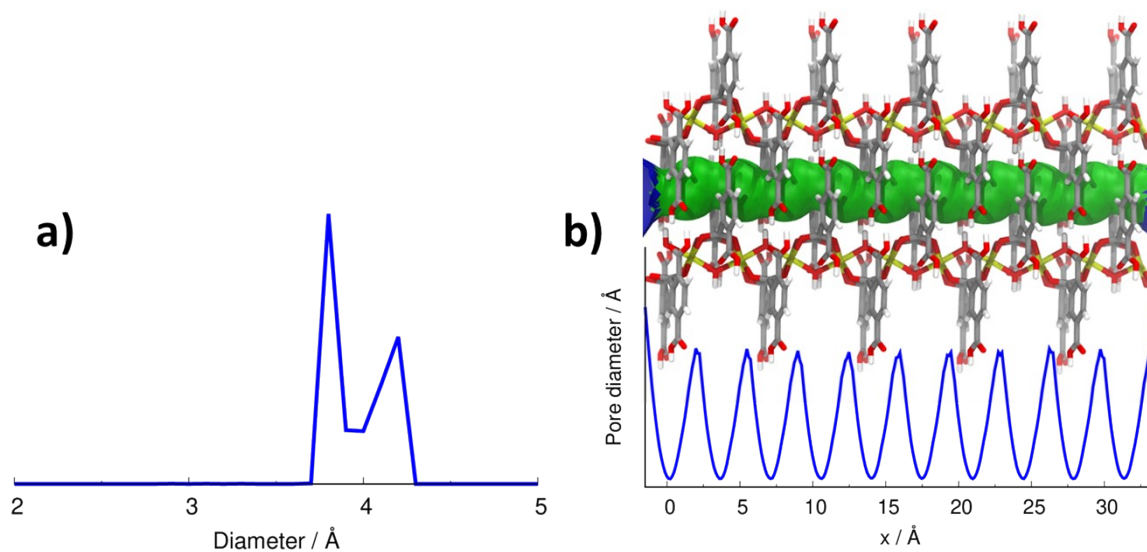


Fig. S8. a) Pore size distribution of the MIL-178(Fe) derived from the DFT optimized geometry and b) shape of the 1-D channel along x-direction.

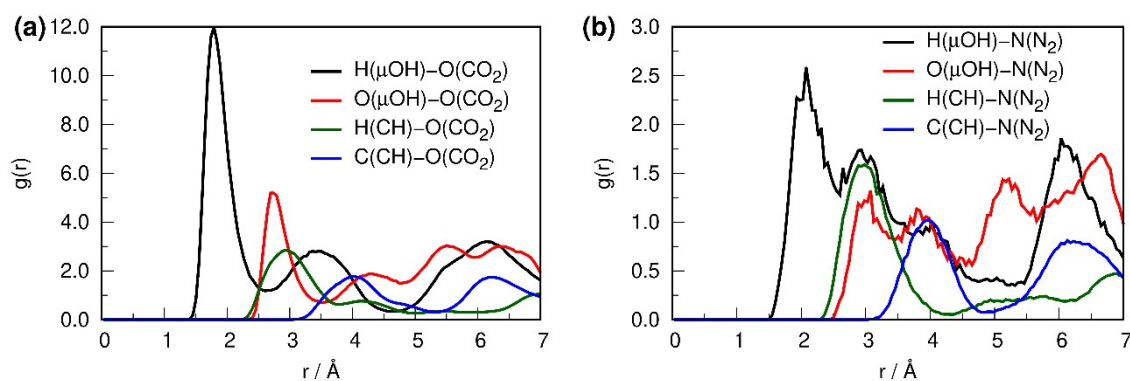


Fig. S9. Intermolecular radial pair distribution functions of MIL-178(Fe) surface atoms and adsorbed CO₂(a) and N₂(b) molecules.

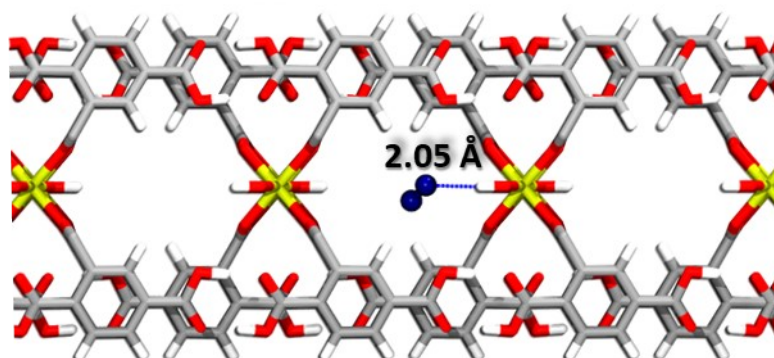


Fig. S10. Microscopic view of the preferential sitings of N₂ molecules in the 1-D channel of MIL-178(Fe) obtained from GCMC simulation performed for single component N₂ molecules at $P = 1$ bar and $T = 303$ K.

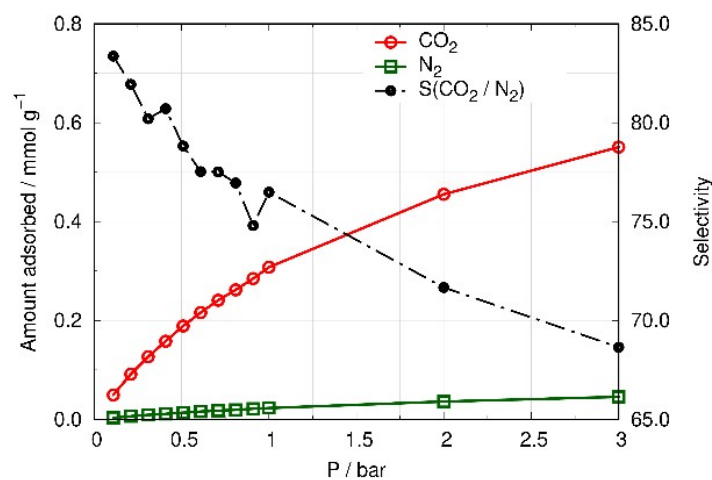


Fig. S11. GCMC calculated co-adsorption isotherms for 15/85 molar compositions of CO₂/N₂ mixture in MIL-178(Fe) at $T = 303$ K.

V-Pressure-dependent PXRD under CO₂.

Experimental. The sample was activated overnight at 70°C with a turbomolecular pump ($\sim 10^{-7}$ mbar) and then transferred to an argon-filled glovebox (0.1 ppm H₂O, 0.4 ppm O₂), where it was loaded into a sapphire capillary. The capillary, embedded in a sample holder was removed from the glovebox and immediately connected to the gas loading system, followed by immediate exposure to vacuum for one hour, before running the diffraction experiment. Two adsorption/desorption cycles were measured from vacuum to 45 bar CO₂ (CO₂ N50, Air Liquide, purity >99.999%), using a Rigaku Mo rotating anode ($\lambda = 0.71073\text{\AA}$), XENOCS focusing mirror and a MAR345 image plate detector.

Data treatment. 2D data were calibrated with LaB₆, sapphire spots of the capillary were masked and the rest of the data was integrated with the Fit2D software, followed by addition of the estimated $\sigma(l)$ for each 2θ step. Localization of CO₂ was performed using FOX software starting from the .cif file of the as-synthesized MOF. The guest solvent molecules (ethanol) were removed to create the structure with empty pores. Then, a rigid body of CO₂ was added, with a 180° angle constraint on the O8-C10-O9 angle and C=O bond distances of 1.16 Å. The positions and occupancies of the atoms of the MOF were fixed, whereas the ones of the CO₂ rigid body were allowed to be optimized. The crystal and powder patterns were optimized by simulated annealing to determine the occupancy and position of the CO₂ molecule. Once CO₂ was located, the Rietveld refinement of the model was done for each powder pattern in a sequential mode, using Fullprof. We optimized the cell parameters, zero shift, W, U, Gaussian/Lorentzian peak shape (pseudo-Voigt function), asymmetry parameters and background. Sequential Rietveld refinement was applied on the pressure-dependent data to determine the occupancy of CO₂ at each pressure. The obtained occupancy was plotted as a number of CO₂ molecules per Fe atom at each pressure, obtaining PXRD-determined sorption isotherms (see Fig.S12). The data points were fitted by a Langmuir-type isotherm with the help of the Origin software.

Langmuir equation:

$$Occupancy = C \times \frac{K \times p}{1 + K \times p}$$

Where C (value at saturation) and K are determined by the fitting of the data points, and p is the experimental pressure.

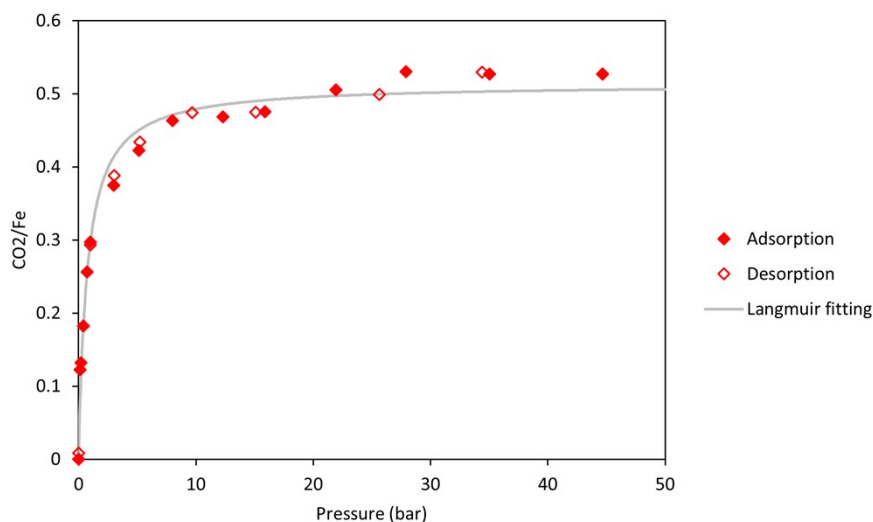


Fig. S12: PXRD-determined sorption isotherms of MIL-178(Fe)-RT (closed symbols = adsorption points, empty symbols = desorption points), together with Langmuir fitting (grey line).

VI – Experimental co-adsorption

The co-adsorption experimental measurements have been carried out using a homemade volumetric apparatus as shown in Fig. S13. This device is used to carry out isotherm (from 298 to 353 K) and isobaric (from 1 to 9.5 bar) measurements thanks to a cylinder piston that replaces the pressure cell. The cylinder piston enables to change the total volume accessible to the gas to set the pressure during adsorption.

Before adsorption, the gas mixture is homogenized by a circulation pump. When the equilibrium is reached (constant gas composition (analyzed by gas chromatograph coupled with TCD Agilent-GC 6890), pressure (Endress-Hauser: 0-1000 kPa Cerabar PMP 731) and temperature (Pt100 probe)), the volume, the temperature, the pressure and the gas composition (at least 5 analyses) are recorded. With an appropriate equation of state²¹ the number of moles of each gas component is determined. Then, the gas mixture goes to the adsorption cell. During this adsorption phase, the cylinder piston allows to reduce the volume to keep the pressure constant. When the equilibrium is reached (constant gas composition, pressure, temperature and volume), the same measurements are made in order to determine the number of moles of each gas component with the same equation of state after adsorption. By difference, the numbers of adsorbed moles are calculated. More information about this experimental device are available in previous papers.^{22,23}

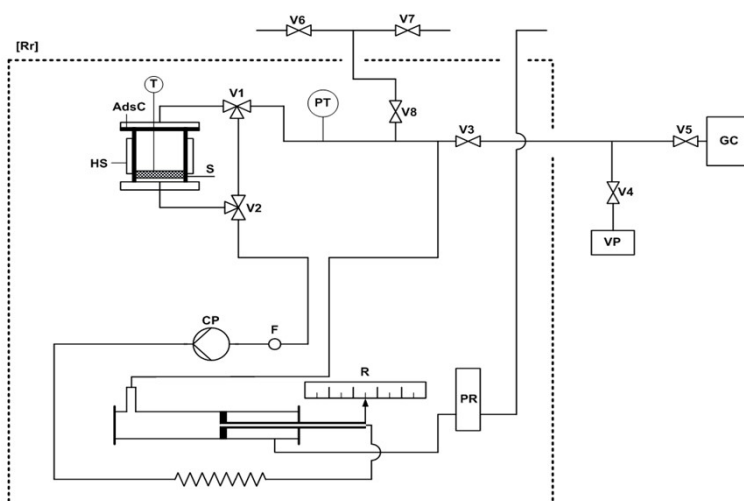


Fig. S13. Experimental device for isotherm and isobaric co-adsorption measurements.

Table S2. Comparison of the CO₂/N₂ selectivity for different materials with moderate heat of adsorption (Q_{st} CO₂ <40 kJ.mol⁻¹).

| Material | CO ₂ /N ₂ selectivity (15 :85) at 1 bar | reference |
|---|---|---|
| [Cu ₂ (4-TPOM)(3,7-DBTDC) ₂] | 883 (298 K) | <i>Inorg Chem</i> , 2021, 60 , 5071-5080 |
| NJU-Bai51 | 545.7 (298 K) | <i>Chem. Commun.</i> , 2019, 55 , 3477-3480 |
| NJU-Bai26 | 366 (298 K) | <i>Inorg. Chem.</i> , 2019, 58 , 13836-13842 |
| NJU-Bai27 | 217 (298 K) | |
| UTSA-16 | 314.7 (296 K) | <i>Nat. Commun.</i> , 2012, 3 , 954 |
| Zn ₂ (bpdC) ₂ (bpee) | 294 (298 K) | <i>Chem. – Eur. J.</i> , 2010, 16 , 13951-13954 |
| NJU-Bai35 | 275.8 (298 K) | <i>J. Am. Chem. Soc.</i> 2018, 140 , 17825-17829 |
| NJU-Bai49 | 166.7 (298 K) | <i>Inorg. Chem.</i> , 2019, 58 , 2729-2735 |
| IITKGP-11 | 149.07 (295 K) | <i>Inorg. Chem.</i> , 2019, 58 , 11553-11560 |
| IITKGP-5a | 147.8 (295 K) | <i>Dalton Trans.</i> , 2017, 46 , 15280-15286 |
| IISERP-MOF26 | 145 (298 K) | <i>Chem. Asian J.</i> , 2019, 14 , 3736-3741 |
| SIFSIX-2-Cu-i | 140 (298 K) | <i>Nature</i> , 2013, 495 , 80-84 |
| Zn-MOF-74 | 87.7 (296 K) | <i>Nat. Commun.</i> , 2012, 3 , 954 |
| USTC-253-TFA | 75 (298 K) | <i>ChemSusChem</i> , 2015, 8 , 878-885 |
| {[Zn ₂ (TPOM)(3,7-DBTDC) ₂]·7H ₂ O·DMA} _n | 73.4 (298 K) | <i>ACS Appl. Mater. Interfaces</i> , 2020, 12 , 11724-11736 |
| {[Cd ₂ (TPOM)(3,7-DBTDC) ₂]·6H ₂ O·3DMF} _n | 46.3 (298 K) | |
| ZIF-78 | 50.1 (298 K) | <i>J. Am. Chem. Soc.</i> 2009, 131 , 3875-3877. <i>Acc. Chem. Res.</i> , 2010, 43 , 58-67. |
| IITKGP-13A | 47 (295 K) | <i>Inorg. Chem.</i> , 2020, 59 , 7056-7066 |
| JLU-Liu46 | 42 (298 K) | <i>ACS Appl. Mater. Interfaces</i> , 2017, 9 , 32820-32828 |
| JLU-Liu47 | 45 (298 K) | |
| BUT-11 | 31.5 (298 K) | <i>Inorg. Chem.</i> , 2014, 53 , 9254-9259 |
| BUT-11 (AcOH) | 24.1 (298 K) | |
| UiO-67 (Zr) | 24.5 (298 K) | <i>Inorg. Chem.</i> , 2014, 53 , 679-681 |
| PCN-88 | 15.2 (296 K) | <i>Nat. Commun.</i> , 2013, 4 , 1538. |
| PCN-61 | 15 (298 K) | <i>J. Am. Chem. Soc.</i> , 2011, 133 , 748-751 |
| MIL-96(Al) | 36 (303 K) | <i>Chem. Mater.</i> , 2017, 29 , 10326-10338 |
| UiO-66(Zr)-(COOH) ₂ | 56 (303 K) | <i>Angew. Chem. Int. Ed.</i> , 2013, 52 , 10316-10320 |
| PCN-80 | 12 (296 K) | <i>Angew. Chem. Int. Ed.</i> , 2012, 51 , 1580-1584 |
| Zn ₂ (BTetB)(py-CF ₃) ₂ | 37 (298 K) | <i>J. Mater. Chem.</i> , 2009, 19 , 2131-2134 |
| Cu-BTC | 20 (298 K) | <i>Energy Fuels</i> 2009, 23 , 2785-2789 |
| ZIF-8(Zn) | 8 (298 K) | <i>Chem. Eng. Sci.</i> , 2011, 66 ,4878-4888 |

VII- Characterization of Mixed Matrix Membranes.

Microstructural characterization. PXRD patterns were recorded in a high-throughput D8 Advance Bruker diffractometer with Cu K α 1 radiation ($\lambda = 1.5418 \text{ \AA}$) in transmission mode. Thermogravimetric (TG) analysis was performed using a Mettler Toledo TGA/STDA 851e. Small pieces of membranes (approx. 8 mg) placed in 70 μ l alumina pans were heated under an air flow (40 ml min⁻¹) from 35 to 700°C at a heating rate of 10 °C min⁻¹. SEM images have been recorded on a JEOL JSM-7001F microscope equipped with an X-ray energy-dispersive spectrometry (XEDS) detector with a X-Max SDD (Silicon Drift Detector) by Oxford using gold-coated samples. Fourier transform infrared (FTIR) spectra were recorded with a Nicolet iS5 FTIR Spectrometer (Thermo scientific, USA).

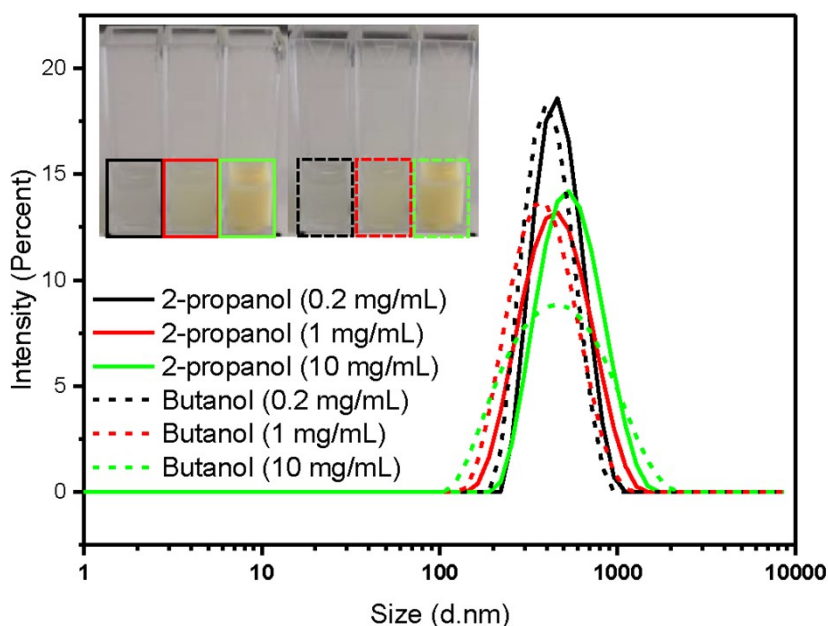


Fig. S14. Size Distribution (diameter in nm) of MIL-178(Fe)-RT in 2-propanol and 1-butanol by dynamic light scattering at different concentrations (0.2, 1 and 10 mg.mL⁻¹). The inset shows photographs of the colloidal solutions of MIL-178(Fe)-RT in 2-propanol or butanol solvents.

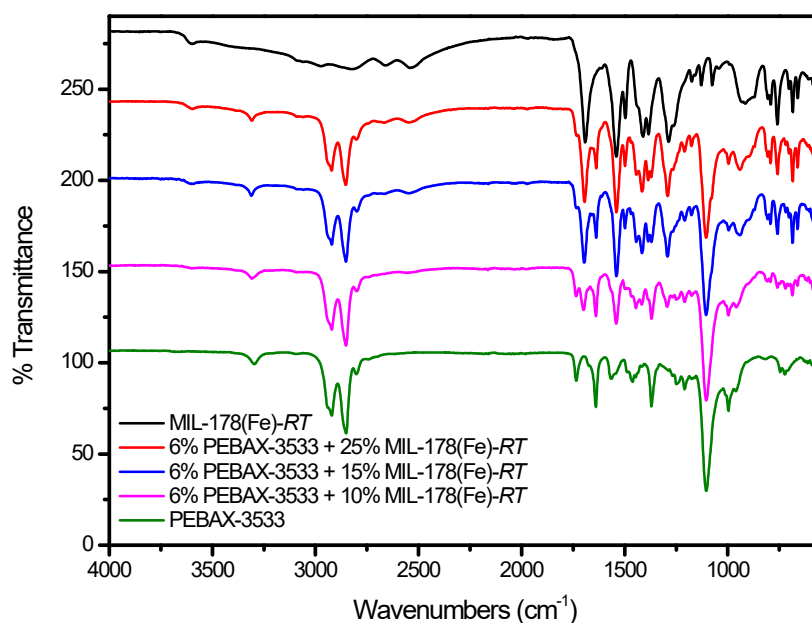
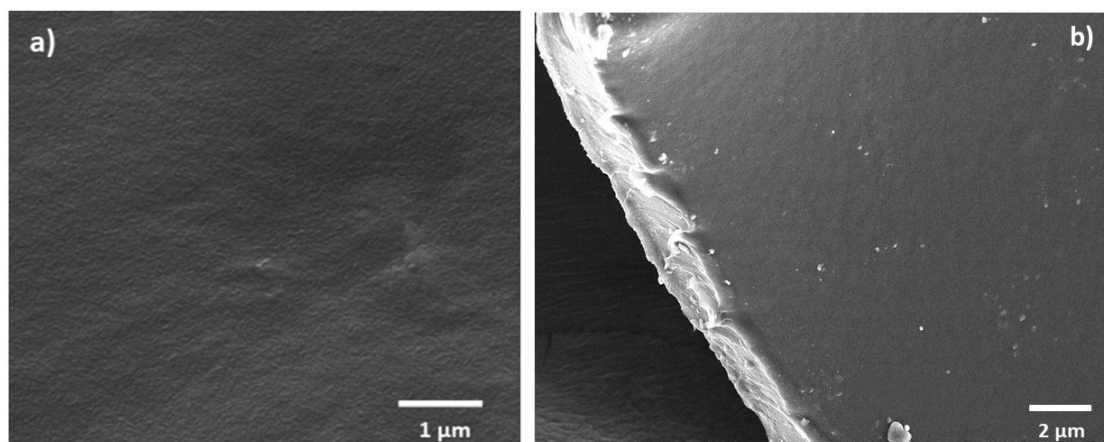


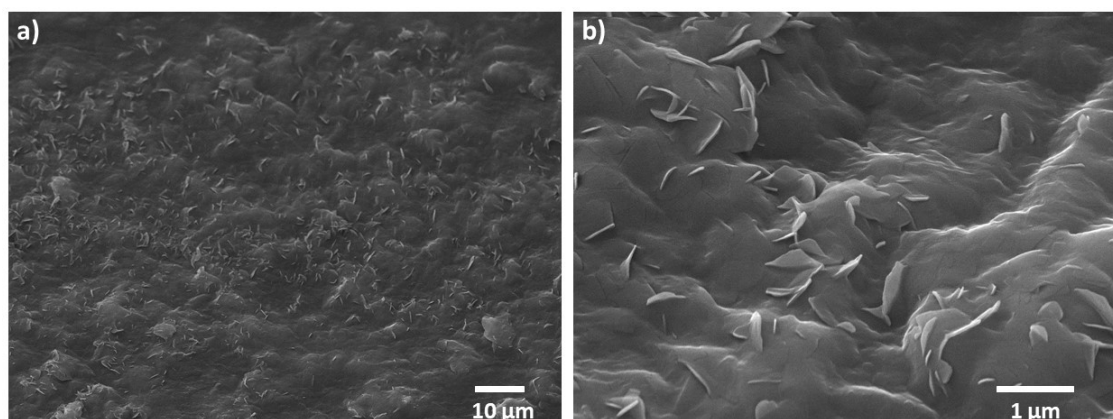
Fig. S15. FT-IR spectra of pure PEBAX and MIL-178(Fe)-PEBAX 3533 MMMs with different MIL-178(Fe)-RT contents.

The FT-IR spectra of MIL-178(Fe)-Pebax-X membranes superimpose well with that of pure MIL-178(Fe) and Pebax[®]-3533. They display a series of vibration bands characteristic of the soft PEO block such as the peak at 1102 cm⁻¹ corresponding to C-O-C group as well as those of the hard polyamide segment of the polymer (i. e. 3295, 1639 and 1735 cm⁻¹ corresponding respectively to the hydrogen bonded -N-H-, H-N-C=O and O-C=O groups). The stretching vibration at 2929 cm⁻¹ indicates the presence of aliphatic -C-H functions. The FT-IR spectra of the membranes present also the characteristic vibration bands of MIL-178(Fe) (i. e. $\nu_s(\text{C}=\text{O}) = 1400 \text{ cm}^{-1}$, $\nu_{as}(\text{C}=\text{O}) = 1543 \text{ cm}^{-1}$ and free carboxylic acid group at 1703 cm⁻¹).

A)



B)



C)

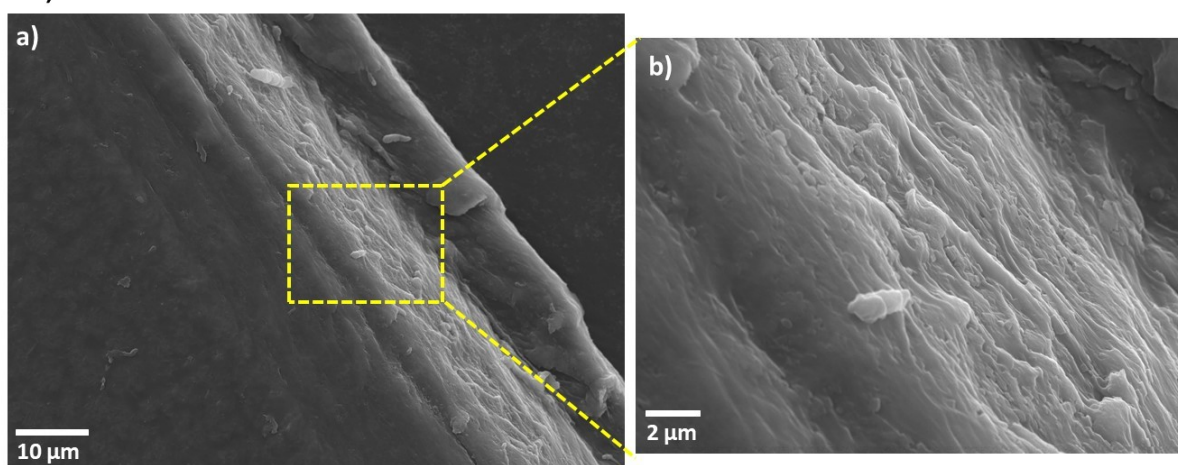


Fig. S16. SEM images of A-a) the top surface and A-b) cross-section pure PEBAx[®]-3533, B-a) and B-b) top surface of MIL-178-Pebax-10 MMM; C-a) and C-b) cross-section images of MIL-178-Pebax-25 MMM

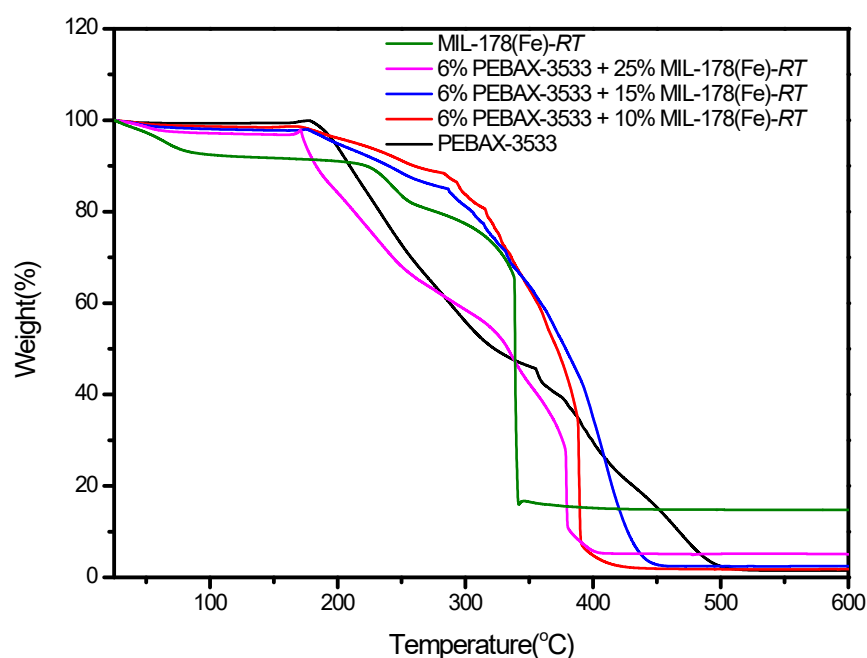


Fig. S17. Thermogravimetric analysis of pure Pebax[®]-3533, MIL-178(Fe)-RT and MIL-178-Pebax-X MMMs with different MIL-178(Fe) contents (X=10, 15 and 25).

Differential scanning calorimetry (DSC) analysis was performed using a Mettler Toledo DSC1 setup. 0.5 mg of sample was deposited and sealed at ambient (25°C) in 40 μ L aluminium crucible with a perforated lid. The reference was an empty crucible (i.e. air) and the heat exchange was calibrated with indium. The thermal protocol was identical for all samples: samples were (1) introduced at room temperature, (2) cooled down to -30 °C in 30 min, (3) equilibrated 2 min at -30 °C and (4) finally heated up to 250 °C at 20 °C/min. To quantitatively analyse the degree of crystallinity of the PTMO phase, the enthalpy of fusion of the PTMO phase was determined by integration of the endothermic peak attributed to the fusion of the PTMO crystalline fraction (i.e. $T_{melting}^{PTMO} \approx 9^{\circ}C$). The degree of crystallinity (χ_c) was then calculated as:

$$\chi_c = \frac{\Delta H_f}{\Delta H_f^*} \times 100$$

where ΔH_f (J/g) is the enthalpy of fusion of the PTMO phase and ΔH_f^* (J/g) is the enthalpy of fusion when the polymer phase is purely crystalline as obtained from the literature ($\Delta H_f^* \approx 200$ J/g). I. J. Bowman, D. S. Brown, R. E. Wetton, *Polymer*, 1969, **10**, 715 - 718.²⁴

25

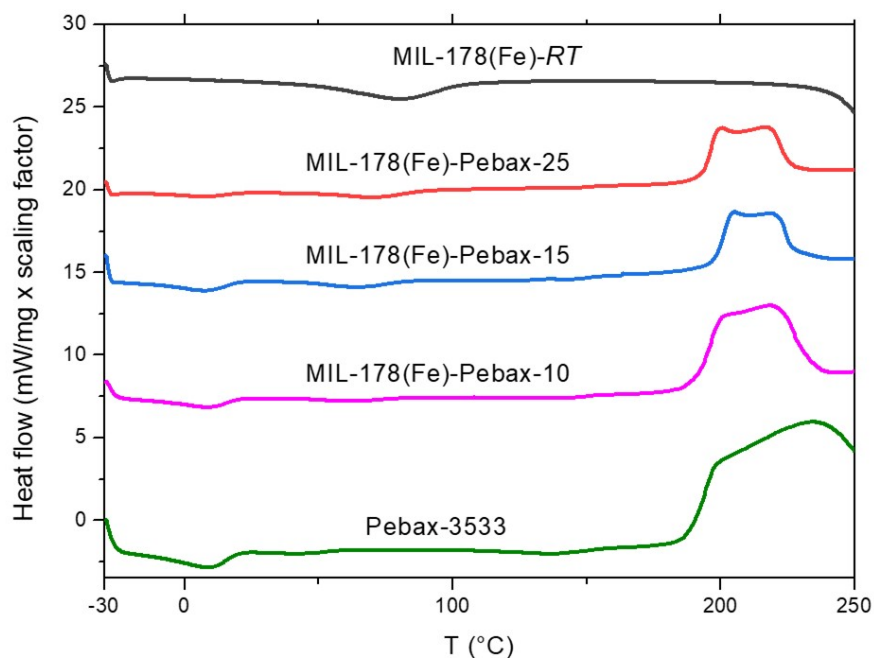


Fig. S18. DSC curves of neat Pebax®-3533 and typical MIL-178(Fe)-Pebax-X MMM. The curves are shifted vertically for clarity.

Overall, the curves are characterized by 3 main peaks.

- An endothermic peak located around 11°C corresponding to the melting of the crystalline phases of PTMO. As indicated in the text, the area of this peak decreases with the MIL-178(Fe) filler concentration until it disappears in the absence of polymer.
- An intermediate endothermic peak located around 80°C. We attribute this peak to the departure of the solvent under the effect of heating. This departure is all the more important as the proportion of MIL-178(Fe) filler is high.
- A double exothermic peak at high temperature ($T_1 \approx 200$ °C ; $T_2 \approx 218$ °C). In light of thermogravimetric analysis, we attribute these peaks to the combustion of the diblock copolymer. The area of this double peak decreases with the MIL-178(Fe) filler concentration until it disappears in the absence of polymer.

Tensile tests until failure.

The mechanical tests were carried out at ambient ($T \approx 25$ °C and $HR \approx 40$ %) on a tensile testing machine (Zwick-Roell, Model Z0.5TN), using a 0.5 kN load cell. Hexahedral-shaped specimens, having a calibrated dimension 20 mm x 6 mm x 0.05 mm were cut from the films with a stamp. These samples were held on the machine between pneumatic clamps. Tensile measurements were performed at a constant crosshead displacement rate of 10 mm.min⁻¹. Data acquisition was started as soon as a preload of 0.5 N was reached. The Young's moduli were calculated using the initial elastic segment (i.e. $0 \leq e$ (%) ≤ 10). The stress at break (σ_{break}) and elongation at break (e_{break}) were determined at the blue cross shown in the Fig. S19.

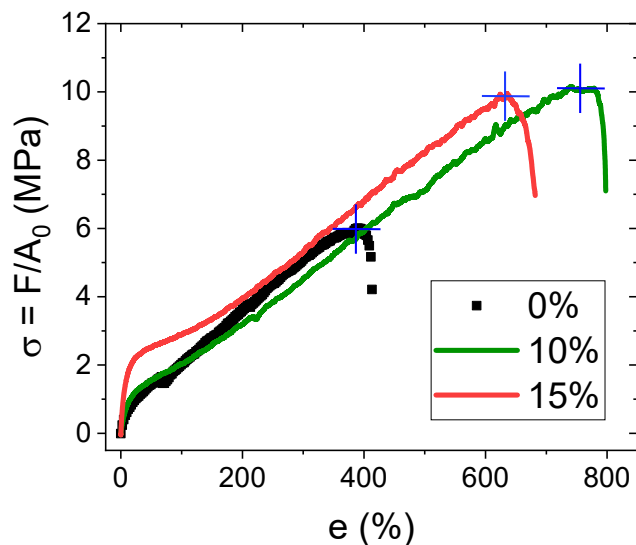


Figure S19. Representative stress-strain curves obtained by tensile testing to failure for MIL-178(Fe)-Pebax-X (X= 10 and 15 wt%) MMMs and a pure Pebax® 3533 membrane (X=0). The blue crosses indicate the position considered for the sample failure.

Table S3. Young moduli (E), Stress at break (σ_{break}) and elongation at break (e_{break}) of the MIL-178(Fe)-Pebax-X MMMs with X = 10 and 15wt% and of a pure Pebax® 3533 membrane (X=0).

| membranes | E, MPa | σ_{break} , MPa | e_{break} , % |
|-------------|--------|------------------------|-----------------|
| Pebax® 3533 | 5.5 | 6 | 394 |

| | | | |
|-----------------------|------|------|-----|
| MIL-178(Fe)-Pebax -10 | 7.1 | 10.1 | 758 |
| MIL-178(Fe)-Pebax -15 | 17.2 | 9.8 | 632 |

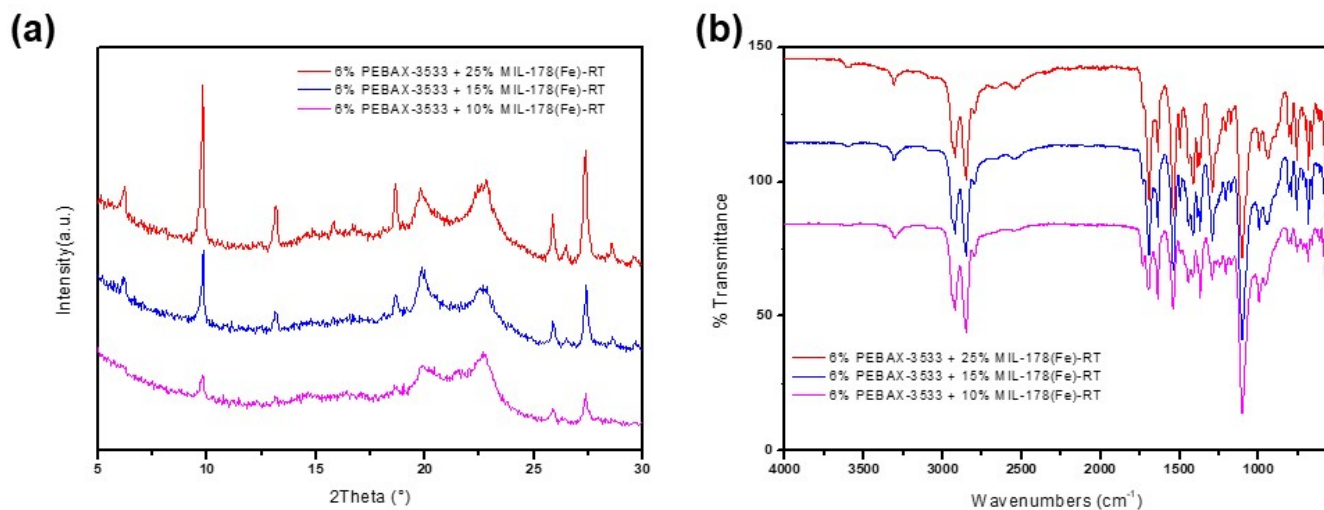


Figure S20. (a) PXRD pattern and (b) FT-IR spectra MIL-178(Fe)-Pebax-X (X= 10, 15 and 25 wt%) MMMs after ageing under humid ambient conditions for 8 months.

N₂ and CO₂ separation experiments.

Gas chromatography was used for gas permeation analysis by an Agilent 3000A micro-gas chromatograph. The separation of the CO₂/N₂ mixture was performed in the experimental system that is schematically presented in Fig. S19. The membranes were cut and placed in a module consisting of two stainless steel pieces and a 316LSS macroporous disc support (Mott Co.) with a 20 μm nominal pore size. Membranes, 2.12 cm² in area, were gripped inside with Viton O-rings. To control the temperature of the experiment, which influences gas separation, the permeation module was placed in an UNE 200 Memmert oven. Gas separation measurements were carried out by feeding the post-combustion gaseous mixture of CO₂/N₂ (15/85 cm³(STP) min⁻¹) at an operating pressure of 3 bar and 35 °C to the feed side, controlled by two mass-flow controllers (Alicat Scientific, MC-100CCM-D). The permeate side of the membrane was swept with 2 cm³(STP) min⁻¹ of He, at atmospheric pressure (approx. 1 bar) (Alicat Scientific, MC-5CCM-D). Concentrations of N₂ and CO₂ in the outgoing streams were analysed online by an Agilent 3000A micro-gas chromatograph. Permeability was calculated in Barrer (10⁻¹⁰ cm³ (STP) cm cm⁻² s⁻¹ cm Hg⁻¹) once the steady state of the exit stream was reached (at least after 3 h). The separation selectivity was calculated as the ratio of permeabilities of CO₂ over permeabilities of N₂. Improvement of the membrane performance compared to bare membrane was calculated following Eq. S1.

$$\text{Improvement} = \frac{\text{Performance of a MMMs} - \text{Performance of bare membrane}}{\text{Performance of bare membrane}} \times 100 \% \quad \text{Eq. S1}$$

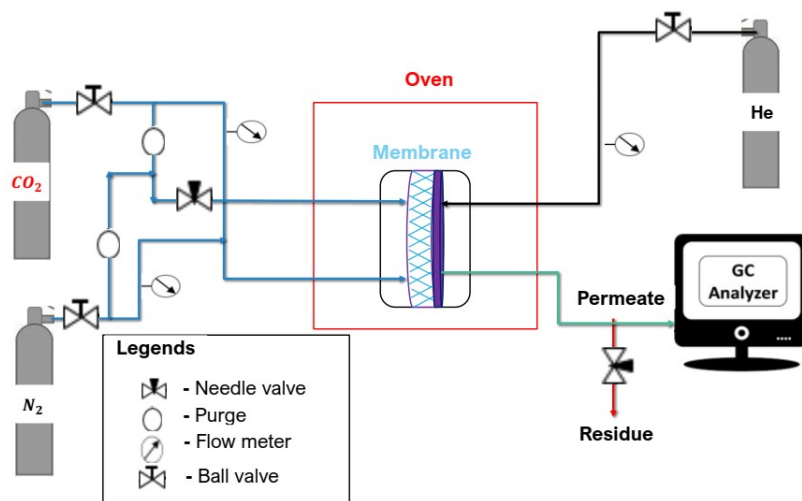


Fig. S21. Schematic representation of GC module for permeation analysis

Table S4. Mixture permeation analysis results of the membranes with filler loading in the polymer matrix

| MIL-178(Fe) content (wt. %) | P CO ₂ (Barrer) | Selectivity (CO ₂ /N ₂) |
|--------------------------------|----------------------------|--|
| 0 | 82 ± 6 | 9 ± 0.7 |
| 5 | 140 ± 15 | 11 ± 4 |
| 7.5 | 158 ± 7 | 14 ± 3.5 |
| 10 | 165 ± 4 | 16 ± 0.7 |
| 12.5 | 172 ± 5 | 15 ± 0.5 |
| 15 | 210 ± 15 | 14 ± 0.7 |
| 20 | 196 ± 20 | 14 ± 0.1 |
| 25 | 175 ± 14 | 10 ± 0.7 |

Time lag permeation experiments

The membranes were cut into 3.2 cm² in area, placed in a module, consisting of two stainless steel pieces and a 316LSS macroporous disc support (Mott Co.) with a 20 μm nominal pore size, gripped with Viton O-rings. To control the temperature of the experiment, which influences gas separation, the permeation module was placed in a Memmert oven (Model: 30-1060). Single gas separation measurements were carried out by feeding N₂ first and then CO₂ at an operating pressure (3 bar upstream pressure and vacuumed at the downstream) and 35 °C. Corresponding upstream and downstream pressure was measured which was used to calculate concentrations of N₂ and CO₂ in the downstream. Permeability was calculated in Barrer (10⁻¹⁰ cm³ (STP) cm cm⁻² s⁻¹ cm Hg⁻¹), diffusivity in cm²/s, and solubility in (cm³(STP)/(cm³ cmHg)) once the steady state of the exit stream was reached. The separation selectivity was calculated as the ratio of permeability of CO₂ over permeability of N₂.

Table S5. CO₂/N₂ permeation results at 35 °C for pure Pebax[®] 3533 membrane and MIL-178(Fe)-Pebax -10 MMM. Comparison between single gas permeabilities (time lag) and 15/85 CO₂/N₂ mixture permeabilities and the corresponding CO₂/N₂ ideal and separation selectivities.

| Pure Pebax [®] 3533 | MIL-178(Fe)-Pebax -10 MMM |
|------------------------------|---------------------------|
|------------------------------|---------------------------|

| Parameter | Mixture separation | Time lag | Mixture separation | Time lag |
|--|--------------------|------------------------|--------------------|------------------------|
| <i>CO₂ permeability (Barrer)</i> | 83 ± 6 | 96 | 165 ± 4 | 126 |
| <i>CO₂ diffusivity (cm²/s)</i> | | 1.3 × 10 ⁻⁷ | | 3.8 × 10 ⁻⁸ |
| <i>CO₂ solubility (cm³(STP)/(cm³·cmHg))</i> | | 7.3 × 10 ⁻² | | 3.3 × 10 ⁻¹ |
| <i>N₂ permeability (Barrer)</i> | 9.2 | 9.5 | 10.3 | 6.9 |
| <i>N₂ diffusivity (cm²/s)</i> | | 1.1 × 10 ⁻⁶ | | 3.9 × 10 ⁻⁷ |
| <i>N₂ solubility (cm³(STP)/(cm³·cmHg))</i> | | 8.2 × 10 ⁻⁴ | | 1.7 × 10 ⁻³ |
| <i>Selectivity CO₂/N₂</i> | 9 ± 0.7 | 10 | 16 ± 0.7 | 18 |

References

- ¹ J. Teillet, F. Varret, unpublished homemade Mosfit program Université du Mans France
- ² M. Sanselme, J.M. Grenèche, M. Riou-Cavellec, G. Férey *Solid State Sci.*, 2004, **6**, 853-858.
- ³ M. Cavellec, D. Riou, J.M. Grenèche and G. Férey *Inorg. Chem.*, 1997, **36**, 2187-2190.
- ⁴ J. VandeVondele, M. Krack, F. Mohamed, M. Parrinello, T. Chassaing, J. Hutter, *Comput. Phys. Commun.*, 2005, **167**, 103-128.
- ⁵ J. Hutter, M. Iannuzzi, F. Schiffmann, J. VandeVondele, *Interdiscip. Rev. Comput. Mol. Sci.*, 2014, **4**, 15-25.
- ⁶ The CP2K developers group <http://www.cp2k.org> (accessed Feb 10, 2019).
- ⁷ J. P. Perdew, K. Burke, M. Ernzerhof, *Phys. Rev. Lett.*, 1996, **77**, 3865-3868.
- ⁸ S. Grimme, J. Antony, S. Ehrlich, H. Krieg, *J. Chem. Phys.*, 2010, **132**, 154104.
- ⁹ S. Grimme, *J. Comput. Chem.*, 2004, **25**, 1463-1473.
- ¹⁰ J. VandeVondele, J. Hutter, *J. Chem. Phys.*, 2007, **127**, 114105.
- ¹¹ S. Goedecker, M. Teter, J. Hutter, *Phys. Rev. B*, 1996, **54**, 1703-1710.
- ¹² M. Krack, M. *Theor. Chem. Acc.*, 2005, **114**, 145-152.
- ¹³ C. Hartwigsen, S. Goedecker, J. Hutter, *Phys. Rev. B*, 1998, **58**, 3641-3662.
- ¹⁴ T. A. Manz, T. A. *RSC Adv.*, 2017, **7**, 45552-45581.
- ¹⁵ N. G. Limas, T. A. Manz, *RSC Adv.*, 2016, **6**, 45727-45747.
- ¹⁶ T. A. Manz, N. G. Limas, *RSC Adv.*, 2016, **6**, 47771-47801.
- ¹⁷ Q. Yang, C. Zhong, *J. Phys. Chem. B*, 2006, **110**, 655-658.
- ¹⁸ J. J. Potoff, J. I Siepmann, *AIChE J.*, 2001, **47**, 1676-1682.
- ¹⁹ D. -Y. Peng, D. B. Robinson, *Ind. Eng. Chem. Fundam.* 1976, **15**, 59-64.

-
- ²⁰ T. F. Willems, C. H. Rycroft, M. Kazi, J. C. Meza, M. Haranczyk, *Micropor. Mesopor. Mat.*, 2012, **149(1)**, 134–141.
- ²¹ O. Kunz, W. Wagner, *J. Chem. Eng. Data.*, 2012, **57**, 3032–3091.
- ²² N. Heymans, B. Alban, S. Moreau, G. De Weireld, *Chem. Eng. Sci.*, 2011, **66**, 3850–3858.
- ²³ P. Billemont, N. Heymans, P. Normand, G. De Weireld, *Adsorption*, 2017, **23**, 225–237
- ²⁴ I. J. Bowman, D. S. Brown, R. E. Wetton, *Polymer*, 1969, **10**, 715-718.
- ²⁵ E.V. Konyukhova, A.I. Buzin, Y.K. Godovsky, *Thermochimica Acta*, 2002, 391, 271–277.